Large eddy simulation of a plane turbulent wall jet

A. Dejoan[a)] and M. A. Leschziner[b)]
Department of Aeronautics, Imperial College London, London SW7 2AZ, United Kingdom

The mean-flow and turbulence properties of a plane wall jet, developing in a stagnant environment, are studied by means of large eddy simulation. The Reynolds number, based on the inlet velocity U_o and the slot height b, is $R_e=9600$, corresponding to recent well-resolved laser Doppler velocimetry and pulsed hot wire measurements of Eriksson *et al.* The relatively low Reynolds number and the high numerical resolution adopted (8.4 million nodes) allow all scales larger than about 10 Kolmogorov lengths to be captured. Of particular interest are the budgets for turbulence energy and Reynolds stresses, not available from experiments, and their inclusion sheds light on the processes which play a role in the interaction between the near-wall layer and the outer shear layer. Profiles of velocity and turbulent Reynolds stresses in the self-similar region are presented in inner and outer scaling and compared to experimental data. Included are further results for skin friction, evolution of integral quantities and third-order moments. Good agreement is observed, in most respects, between the simulated flow and the corresponding experiment. The budgets demonstrate, among a number of mechanisms, the decisive role played by turbulent transport (via the third moments) in the interaction region, across which information is transmitted between the near-wall layer and the outer layer.

I. INTRODUCTION

The wall jet is a flow which is both practically important and fundamentally interesting. The most frequent engineering applications featuring wall jets are encountered in cooling, heating, demisting and drying of surfaces. A particular important example is the injection of wall jets parallel to the inner surface of a combustion chamber, designed to protect it from the hot combustion products. A wall jet is also formed as a consequence of jet impingement on a surface. This arises, for example, in the context of heating or annealing of metal and glass plates during manufacture. In all these applications the turbulence structure of the wall jet, especially that close to the surface, is a key issue to the jet's thermal performance.

From a fundamental point of view, the most distinctive and interesting feature of a wall jet is the interaction between the near-wall layer, having the characteristics of a boundary layer, with an outer free shear layer evolving from a separation line at the nozzle exit. These two flow components possess quite different characteristics, in terms of length scales, turbulence anisotropy and structure, and the interaction between them is of particular interest. An intriguing feature of the three-dimensional (finite width) wall jet is the very rapid spanwise spread, relative to that normal to the wall — an experimental observation that is associated with the highly anisotropic turbulence transport in the jet and which has been extremely difficult to replicate computationally with any but the most elaborate forms of second-moment closure (Craft *et al.*[1]).

The first substantive state-of-the-art review on wall jets

was undertaken by Launder and Rodi.[2,3] This summarizes all the main observations emerging from various experimental studies (Tailland and Mathieu[4] and Irwin[5]), including the linear growth of the outer shear layer, at a rate some 30% lower than that of a free shear layer, the displacement of the position of the zero shear stress from the position of the maximum velocity and the restricted near-wall region in which the log-law profile applies. Significant uncertainties associated with three-dimensional contamination and limitations of the hot-wire technique were at that time said to inhibit definitive analysis and conclusions. In particular, insufficient near-wall resolution and the lack of data for the wall-shear stress, wall-normal and spanwise intensities, as well as lack of accuracy of the shear-stress data, were highlighted as being major problems. A number of studies in the 1990s, using both improved hot-wire and, increasingly, laser Doppler anemometry resulted in substantially improved data being obtained (Wygnanski *et al.*,[6] Schneider and Goldstein,[7] Abrahamsson *et al.*[8] and Eriksson *et al.*,[9] Venas *et al.*[10]). Most recently, Eriksson[11] has reported detailed experimental data up to and including fourth-order moments.

All experiments suggest that the plane wall jet becomes self-similar at a streamwise distance of order greater than 20 discharge-nozzle heights. This conclusion rests, principally, on the observation that the spreading rate, expressed in terms of jet half-width, asymptotes to a linear law. Thus, the use of outer-flow scaling has been observed to collapse both the mean velocity and the Reynolds stresses sufficiently far downstream. On the other hand, inner-flow scaling, based on the shear velocity and the universal wall distance, collapses the profiles of the near-wall shear layer, as observed in a near-equilibrium boundary layer. However, leaning on the more recent experimental data for wall jets, George *et al.*[12] have demonstrated that neither inner scaling nor outer scal-

[a)]Electronic mail: ...
[b)]Electronic mail: mike.leschziner@imperial.ac.uk

ing can be used exclusively to collapse the profiles in near-wall and outer shear layer, respectively, except in the limit of infinite Reynolds number, the obstacle to this collapse being the interaction region which remains Reynolds-number dependent. The implication is that the scaling of the outer flow, allowing a proper self-similar representation to be achieved, has to involve inner-layer scales (e.g., the friction velocity).

The correct representation of the development of the plane wall jet towards the self-similar state and the behavior in the interaction region are the primary criteria for judging the performance of statistical closure models. Early computational studies of the plane turbulent wall jet, using RANS modeling, are reviewed by Launder and Rodi,[2,3] while more recent work is surveyed by Gerodimos and So.[13] Although most models, if well calibrated for thin-shear flow, give a broadly correct behavior of the gross flow features, the reviews demonstrate that only full second-moment closure gives a credible description of the processes within the interaction region, specifically the displacement between the zero-shear-stress and zero-velocity-gradient locations. Thus, yet again, the message is that the interaction mechanisms in this region and their effects on the flow components on either side are the most challenging and interesting aspects of the wall jet.

Although past experimental studies provide a wealth of increasingly accurate data on wall jets, there are a number of incentives for undertaking further studies exploiting current simulation capabilities. One is to strengthen conclusions on scaling and similarity; another is to study the initial development of the jet, including transitional features. Perhaps the most important motive, however, is to determine the budgets of the turbulent stresses. These budgets are, arguably, the key to gaining an understanding of what governs the interaction between the outer and the inner layers. They also provide the foundation for the most searching examination of turbulence closures intended to represent this interaction. Indeed, the present study is intended to aid this investigation of turbulence models in the post-reattachment recovery region of separated flows, in which a newly evolving boundary layer interacts with a free-shear layer above it. While this type of flow differs in detail from that of a wall jet, the two share the kind of complex interactions that occur in the region within which two very different flow components overlap.

Strictly, the only computational method that is able to give very detailed and physically reliable information of any turbulence flow is direct numerical simulation (DNS). However, the wall jet demands a large computational domain, especially if it is to extend to the self-similar regime, and exhibits a broad range of turbulent scales, spanning transition close to the discharge to fully developed high-Reynolds-number turbulence in the self-similar domain. This makes DNS extremely expensive at elevated Reynolds numbers. To the knowledge of the present authors, DNS has only been used by Wernz and Fasel[14] and Gogineni et al.[15] to study transitional two-dimensional wall jets at low Reynolds number. At practically relevant Reynolds numbers it is necessary to resort to large eddy simulation (LES). This approach is, arguably, an acceptable alternative, provided the resolution penalties can be shown to have a negligible effect on the
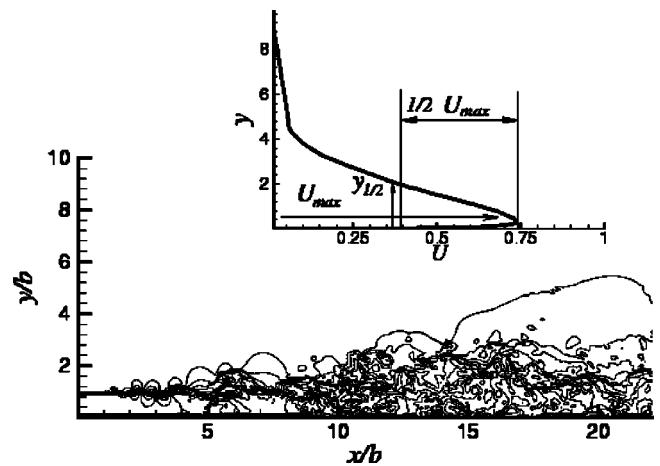

FIG. 1. The turbulent wall jet-typical mean-velocity profile and an instantaneous realization showing transition at $x/b \sim 2$.

principal features of interest. The present paper thus reports a LES study of a plane wall jet at a Reynolds number identical to that in experiments of Eriksson et al., namely $R_e = U_o b / \nu = 9600$, where U_o is the maximum inlet velocity and b is the height of the jet-discharge nozzle. The computational grid has been chosen such that the effect of subgrid-scale modeling is minimized and that almost all the dynamics of the flow are contained in the explicitly resolved scales. The mean flow and the turbulence statistics are directly compared to the experimental data. Also, the budgets of the Reynolds stresses are presented. As noted already, this is especially useful in the context of statistical modeling.

II. COMPUTATIONAL PROCEDURE

A. The numerical method

The computational method rests on a general multiblock finite-volume scheme with nonorthogonal-mesh capabilities (Lardat and Leschziner[16]). The scheme is second-order accurate in space, using central differencing for advection and diffusion. Time-marching is based on a fractional-step method, with the time derivative being discretized by a second-order backward-biased approximation. The flux terms are advanced explicitly using the Adams–Bashforth method. The provisional velocity field is then corrected via the pressure gradient by a projection onto a divergence-free velocity field. To this end, the pressure is computed as a solution to the pressure-Poisson problem by means of a partial-diagonalization technique (Schumann and Sweet[17]) and a V-cycle multigrid algorithm, operating in conjunction with a successive line over-relaxation scheme. The code is fully parallelized and was run on a multi-processor Origin 3800 computer.

B. The flow configuration and computational setup

The flow domain is shown in Fig. 1. It extends from the wall to 10 jet-discharge heights above it and to 22 heights in the streamwise direction ($L_x = 22b$, $L_y = 10b$). The flow is treated as statistically spanwise homogeneous, with the spanwise domain depth L_z being 5.5 jet-discharge heights. The
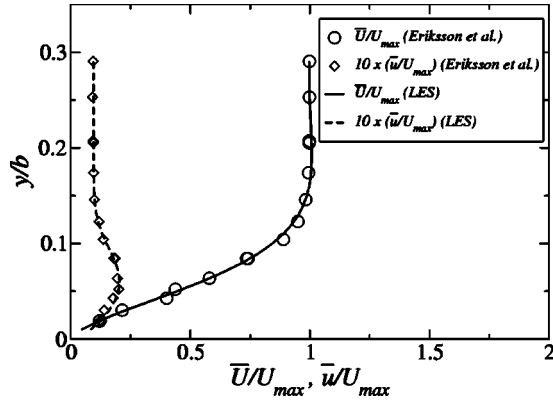
FIG. 2. Mean-velocity and longitudinal turbulence intensity applied at the jet discharge plane $x/b=0$.

FIG. 3. Distance of the wall-nearest cell center from the wall.

vertical boundary above the jet exit is a wall. This computational domain is much smaller than the experimental one, a restriction dictated by computer-resource constraints. Stringent demands on streamwise resolution are posed by the need (and wish) to study the evolution of the wall jet, and these are aggravated by its transitional state in the region $x/b<10$, which has a major effect on the spreading rate, among other flow properties. At the same time, the computational domain had to be extended to a position at which the flow could be regarded as being effectively self-similar. In the experiment, the jet extended to $x/b=700$ downstream of the nozzle, although only the range $x/b<150$ was regarded as free from contamination by the reverse flow in the outer region. The measured data indicated that the flow properties, when appropriately scaled, hardly changed between $x/b=20$ and 40, suggesting that the flow was very close to being self-similar at $x/b=20$. Full self-similarity was observed far downstream, around $x/b=70$. It is this set of observations that led, in the face of the high resolution requirements, to the restriction $x/b=22$. The spanwise domain size in the computation is also much smaller than in the experiment, but here the reduction is inconsequential, because the imposition of spanwise periodicity allowed the simulated flow to attain spanwise homogeneity within a much smaller spanwise distance than was needed in the experiment to secure two-dimensionality. The value of the spanwise depth, $L_z=5.5b$, was chosen such that the velocity fluctuations be decorrelated along this direction.

Jet-inflow conditions are prescribed at the nozzle exit, $x/b=0$, in accordance with the experimental conditions, as shown in Fig. 2. The relative inlet turbulence intensity is low, its maximum value being of order 0.02, and is represented by random isotropic fluctuations with variance consistent with the experimental turbulence level. The inlet flow is, effectively, laminar, perturbed by minor temporal fluctuations.

At the outflow, the convective, non-reflective boundary condition

$$\frac{\partial U_i}{\partial t} + U_c \frac{\partial U_i}{\partial x} = 0 \qquad (1)$$

is applied, where U_c is the local streamwise velocity and x the streamwise direction. Depending on whether U_c is posi-
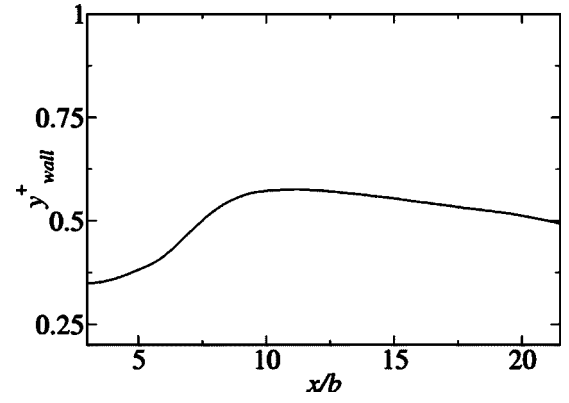
tive or negative, the outflow condition is either determined from (1) or is kept at the value computed at the previous time step.

At the upper boundary, $x/b=10$, a prescribed distribution of entrainment velocity is applied. This is based on Schlichting's semi-analytical solution for a free plane jet:[18]

$$V_{\text{top}} = A \frac{\sqrt{3}}{4} \sqrt{\frac{K}{\sigma x}} (2\eta (1 - \tanh^2 \eta) - \tanh \eta) \qquad (2)$$

where $\eta=\sigma x/y$, $\sigma=7.67$, and $K=\int_{-\infty}^{+\infty} U^2 dy$. To account for differences between the plane and wall jet, the multiplier A is introduced into (2), the value of which has been chosen to match the asymptotic value of the entrainment velocity measured experimentally at a location at the right-hand-side corner of the solution domain. Test computations have shown that the computed flow was essentially unaffected by the value A, as long as the imposed normal velocity at the upper boundary was a small fraction of the inlet velocity U_o. In the present study, $A=3$, which leads to a maximum value of the entrainment velocity of 5% of the maximum inlet velocity U_o. The small upper entrainment velocity applied here can be viewed as equivalent to the weak co-flow introduced in simulations of turbulent free jets (see Da Silva,[19] Le Ribault et al.[20] and Stanley et al.[21]). These authors also reported that there were no effects on the jet dynamics if the lateral boundaries were placed sufficiently far away and the co-flow is small.

In an effort to achieve the best possible resolution, subject to resource constraints, preliminary computations were undertaken with a range of grids. In the present case, the scope for compromise was very limited, because of the need to resolve the transition in both the free shear layer and the boundary layer, as well as the refined interaction processes between the two layers. After some considerable testing, a grid of 420 streamwise nodes, 208 wall-normal nodes and 96 spanwise nodes was used. This gives a total of 8.4 million nodes — a large grid, considering the relatively low Reynolds number. In the wall-normal direction, 100 nodes cover the region $0<y/b<1$, where the outer shear layer interacts strongly with the wall region. The wall-nearest computational node is located at $y^+<1$ (see Fig. 3). In the outer shear layer, the wall-normal grid distance ranges from $\Delta y/b=0.02$ to 0.05 in the region $1<y/b<5$. In the streamwise
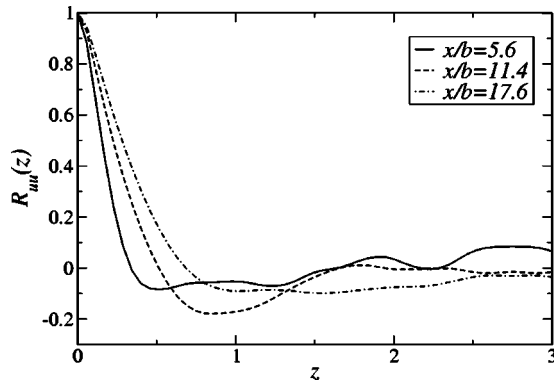
FIG. 4. Spanwise correlation of the streamwise-velocity fluctuation at the location $y/b=1$ for several streamwise x/b positions.

FIG. 6. Ratio of the cell size to the Kolmogorov scale along several streamwise and wall-normal lines.

direction, the cell distance varies between $\Delta x/b=0.06$ to 0.3, with an expansion ratio being lower than 5%. The spanwise box is large enough to secure a decorrelated state of the turbulent fluctuations (see Fig. 4). In this direction, the 96 grid planes are distributed uniformly. In terms of wall coordinates, the resolution in the self-preserving region is $\Delta x^+ \sim 24$ and $\Delta z^+ \sim 23$.

Different subgrid-scale models have been tested. Simulations realized with the Smagorinsky model,[22] the WALE model of Ducros et al.[23] and the dynamic Smagorinsky model of Germano[24] revealed that, despite the fine grid being used, the flow properties in the near-wall region were not entirely insensitive to the subgrid-model used. This sensitivity was observed to express itself especially through differences in the profile of the streamwise turbulent Reynolds stress in the near-wall region. Figure 5 gives a comparison of profiles of the root-mean square (rms) of the streamwise turbulent Reynolds stress obtained in the self-preserving region with the different models tested. The statistics for each model correspond to averages performed over both the spanwise direction and 10 flow-through periods. For the dynamic model—the one actually used for the definitive simulation—averaging was performed over 20 flow-through periods in an effort to maximize the smoothness of the correlations contributing to the budgets of the turbulence energy and the Reynolds stresses. It is observed that, compared to the ex-

periments, the peak intensity in the outer shear layer is well predicted by the WALE and dynamic models, but is slightly too low with the Smagorinsky model. On the other hand, the WALE model predicts an excessively high intensity peak in the near-wall region whereas the Smagorinsky and dynamic models give results in good agreement with the experiment data. These observations lead to the dynamic model being chosen for the computations reported herein. One further reason for this choice is the observation that this model is more appropriate than nondynamic forms for the simulation of transitional flows.

The ratio of grid size to the Kolmogorov length, Δ/η, resulting from the use of the dynamic model is given in Fig. 6 by way of profiles at various $x=$const and $y=$const lines for the grid $420 \times 208 \times 96$. As seen, this ratio is lower than 10 throughout the computational domain. The dissipation rate used to derive the Kolmogorov length in Fig. 6 was computed from the balance of the turbulence-energy budget. This is necessitated by the fact that the dissipation rate cannot be determined explicitly from the simulation itself, as a fraction of it is contained in the subgrid scales. Figure 20 provides an assessment of the proportion that can be extracted explicitly from the simulation. This figure gives the turbulence-energy budget at $x/b=20$ and contains both the dissipation computed from the resolved fluctuating velocity field, ε_c, and the total dissipation, ε, including ε_c and the subgrid scale dissipation as well. As seen, the maximum value of the ratio $\varepsilon/\varepsilon_c$ is of order 2. This is a reliable indicator that the cutoff is in the dissipative range. Also, consistent with above, but not shown here, is that the time-averaged subgrid-scale viscosity was found to be of the same order as the fluid viscosity.

Finally, the spectra of the the streamwise, wall-normal and spanwise velocity fluctuations, in both frequency and spanwise wave number, are given in Fig. 7. The familiar $f^{-5/3}$ decay law is evident in the frequency range $0.1 < fb/U_o < 1$, which corresponds to the inertial subrange. Beyond this range, dissipation is the dominant process, and the decay is at a much faster rate. Both spectra show that the largest frequency and wave number resolved are located in the high-frequency and high wave number zone, associated with the dissipative process. This is yet another indicator of the high resolution of the simulation.
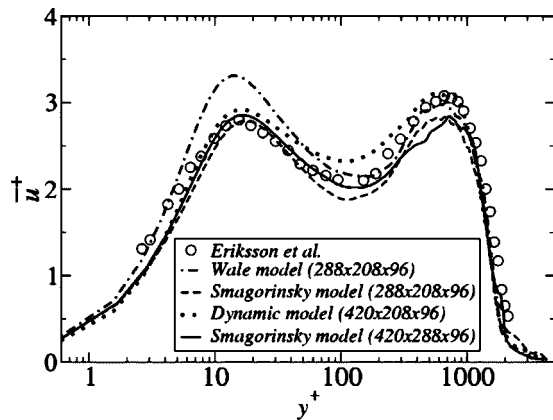

FIG. 5. Profiles of the RMS of streamwise normal stress, scaled with inner variables and computed with different subgrid-scale models at $x/b=20$.
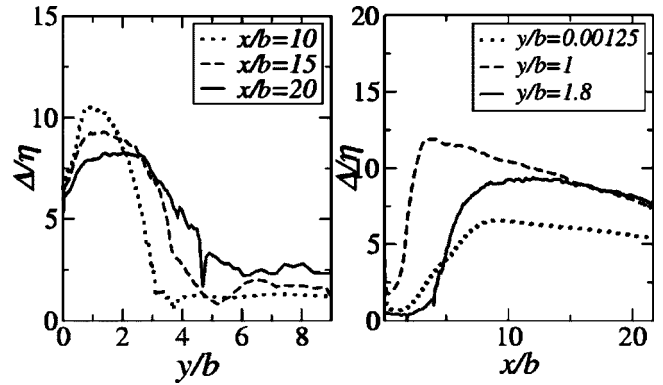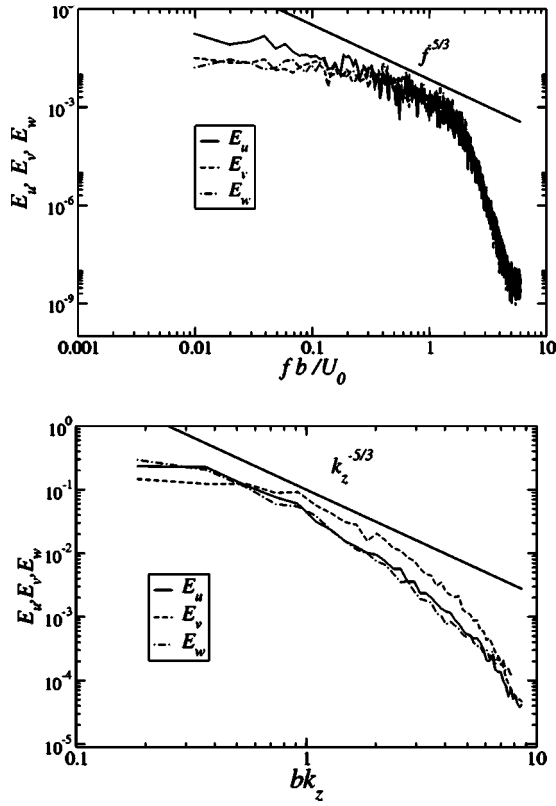
FIG. 7. Frequency and wave-number spectra of the streamwise, wall-normal and spanwise velocity fluctuations at the location $x/b=20$, $y/b=1$.

FIG. 8. Top: growth rate of the wall jet. Bottom: evolution of the wall thickness along the streamwise direction.

III. SCALING OF FLOW VARIABLES

As the wall jet combines a boundary layer and an outer shear layer, which interact strongly, there is clearly a substantial uncertainty on what scaling is appropriate in an effort to bring out any self-similar characteristics of the jet. A reasonable expectation is that inner scaling would be appropriate for the near-wall flow, while outer scaling would apply to integral characteristics and the outer shear layer. However, the interaction between the inner and outer flow invalidates this sharp distinction. The most recent studies on the applicability of various scaling laws have been undertaken by Wygnansky *et al.*,[6] whose experiments were aimed at identifying Reynolds-number effects, and by George *et al.*,[12] who proposed a new similarity theory, which they verified by reference to experimental data provided by Wygnansky *et al.*, Abrahamsson *et al.*[8] and Eriksson *et al.*[9] As noted already, George *et al.* principal conclusion was that no universal scaling exists, except at the infinite-Reynolds-number limit. In the inner layer, the appropriate velocity scale is the friction velocity u_τ, and the length scale is ν/u_τ. In the outer layer, the velocity scale is U_{max}, the velocity maximum, and the length scale is $y_{1/2}$, defined as the distance from the wall to the position at which the mean velocity has declined to half of its maximum value. One important result reported by George *et al.* is that the shear stress in the outer layer scales with u_τ, so that the outer layer is governed by the two velocity scales, U_{max} and u_τ. On the other hand, the normal Reynolds stresses scale only with U_{max} in the outer layer. The interaction region is found to extend from $y^+ \sim 30$ to y^+
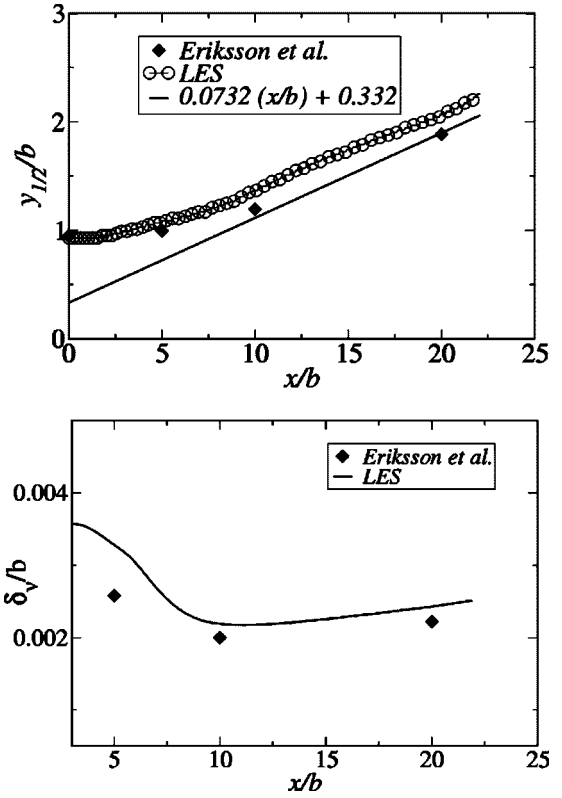
$\sim 0.1\delta^+$, where $y^+ = yu_\tau/\nu$ and $\delta^+ = y_{1/2}u_\tau/\nu$. Using results from the present computation in the beginning of the self-similar region, $x/b=20$, the upper limit $y^+ \sim 0.1\delta^+$ has been estimated to correspond to $y^+ \sim 90$.

In what follows, profiles of flow properties are presented in both inner and outer scaling, in an effort to identify those regions in which one or the other implies self-similarity. However, it is not the purpose of the present study to investigate self-similarity *per se*. Rather, scaling is used principally to examine correspondence with features highlighted by the experiments and to convey confidence in relation to the interpretation of the budgets.

IV. GLOBAL CHARACTERISTICS

The predicted streamwise evolution of length scales characteristic of the outer layer, $y_{1/2}/b$, and inner layer, $\delta_\nu/b = \nu/(u_\tau b)$, is presented and compared to the corresponding experimental variations in Fig. 8. The growth rate of both scales agrees well with the experiment. In particular, the spreading rate of the wall jet beyond $x/b=10$ follows quite closely the linear growth given by Eriksson *et al.* One source for the relatively minor discrepancies is that the details of the transition process in the outer shear layer and especially in the boundary layer are extremely difficult to reproduce with very high accuracy. Transition depends sensitively on the resolution, the perturbations present at the discharge plane and the subgrid-scale model.

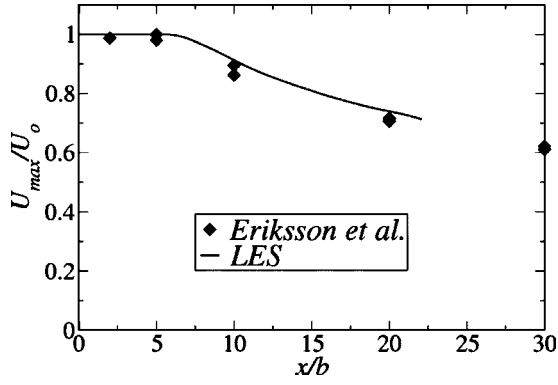As shown in Fig. 9, the predicted streamwise decay of the maximum velocity U_{max} also compares well with the

FIG. 9. Evolution of the maximum longitudinal velocity along the streamwise direction.
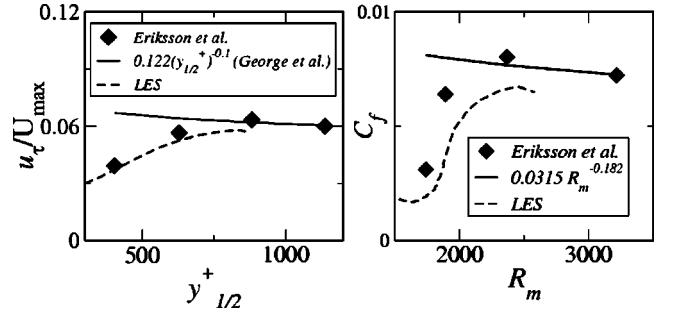

FIG. 10. Left: streamwise evolution of the ratio of the wall shear stress to the maximum velocity. Right: streamwise evolution of the skin-friction coefficient with the Reynolds number $R_m = U_{max} b / \nu$.

experimental data, although lying marginally above it. The fact that both the predicted half-width and the maximum velocity are higher than the respective experimental variations implies that the computation returned a higher streamwise-momentum flux. The source for this difference is suggested by Table I and the bottom plot in Fig. 8, the former reporting the computed and measured values of the friction velocity at two streamwise locations. As seen, the predicted friction velocity is about 10% lower than that recorded experimentally. Although Fig. 10 shows the variation u_τ / U_{max} to agree well with the experiment, this scaling does not convey sensitivity to the level of friction velocity, but rather represents the effect of the wall friction on the variation of the outer scales through the Reynolds shear stress which, as shown by George et al., is Reynolds-number dependent also in the outer region. George et al. further show that u_τ / U_{max} follows a power law in the self-preserving region, which the present results approach at the location $x/b = 20$. Of greater relevance to the issue of excessive half-width is the fact that the predicted skin friction coefficient $C_f = \tau_w / 0.5 \rho U_{max}^2$, as a function of the Reynolds number $R_m = U_{max} y_m / \nu$, is lower than the experimental data and also lower than the power law proposed by Bradshaw and Gee[25] for high Reynolds numbers. This is, thus, consistent with the higher levels of half-width and maximum velocity predicted.

A. Inner-scaled property profiles

Figures 11–16 present various profiles of mean-velocity and turbulent correlations, all scaled with the inner variables u_τ and ν/u_τ, at the streamwise locations $x/b = 10$ and $x/b = 20$. The predicted variations are generally found to agree well with the corresponding experimental data.

Figure 11 shows the velocity maximum to occur at $y^+ = 137$. At the position $x/b = 10$, the flow is still affected by

TABLE I. Comparison of the wall-friction velocity between the LES and experiments at $x/b = 10$ and 20.

	u_τ / U_0 (Eriksson et al.)	u_τ / U_0 (LES)
$x/b = 10$	0.052 44	0.046 92
$x/b = 20$	0.047 72	0.042 86

transition and has clearly not reached the self-similar state. In particular, the slightly negative value of the normal velocity $\bar{V}^+$ near the wall is associated with this transition. The transitional nature of the flow at this position is recognized from Fig. 1 which gives instantaneous streamwise velocity iso-contours. The predicted velocity $\bar{U}^+$ is somewhat higher than that measured in the inner and interaction regions, again reflecting the somewhat low level of wall-shear stress discussed earlier.

Figure 12 provides magnified views of the streamwise velocity in the near-wall region. There is a narrow strip, extending from $y^+ \sim 30$ up to $y^+ \sim 80$, in which a log-law $\bar{U}^+$ can be said to exist. Very near the wall, the velocity profiles
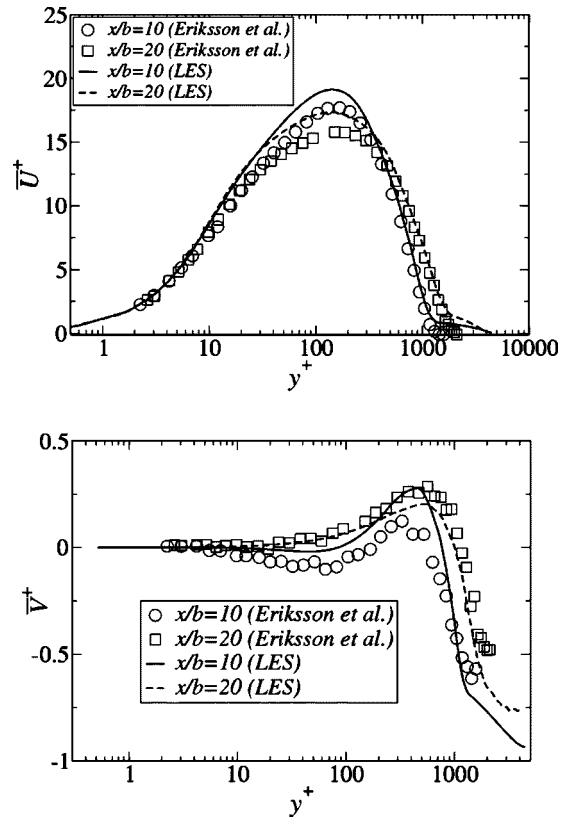

FIG. 11. Profiles of the streamwise and wall-normal velocity at the locations $x/b = 10$ and 20, scaled with inner variables.
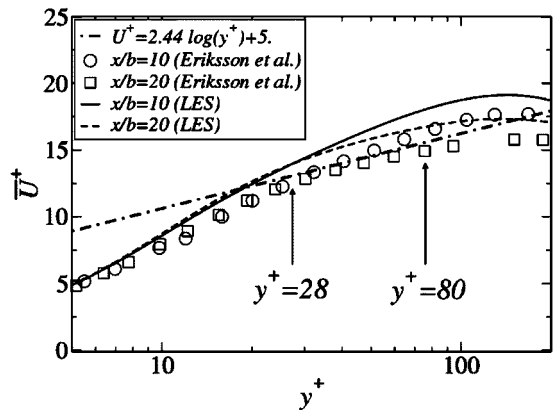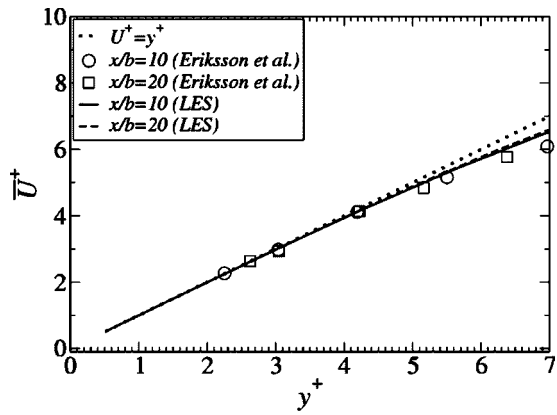
FIG. 12. Linear and log law profiles of the streamwise velocity at the locations $x/b = 10$ and 20, scaled with inner variables.
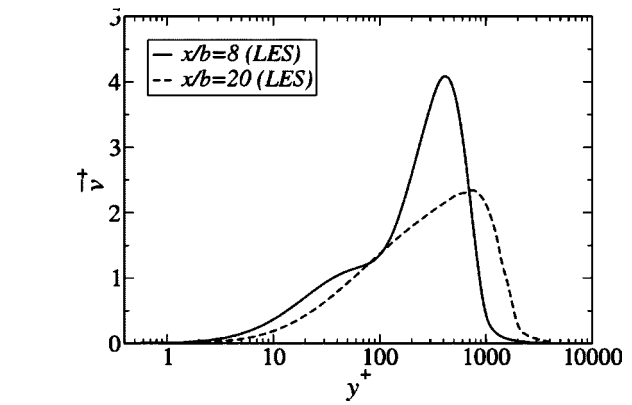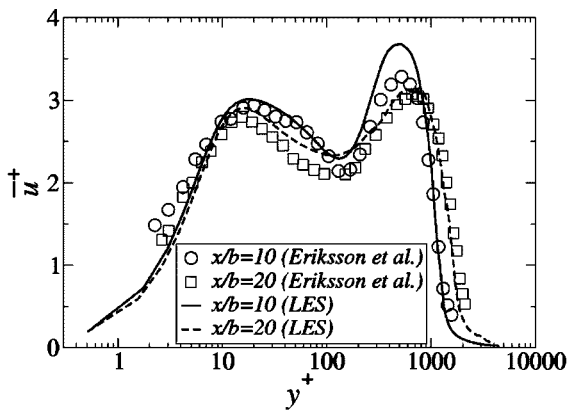

FIG. 14. Comparison of the profiles of the rms of the transverse normal stress in the transitional and self-similar regions, scaled with inner variables.

are, as expected, linear, but begin to deviate from this linear behavior beyond $y^+ = 4$ instead of $y^+ = 8$ in a standard boundary layer.

Profiles of the rms of the normal velocity fluctuations and of the turbulence energy are shown in Fig. 13. All profiles but that for the wall-normal fluctuation display a twin-peak behavior, with the trough being very close to the location of maximum velocity, where the production rate of turbulence by shear straining tends to vanish. The two peaks are located at distances from the wall which compare well with the experiments, namely $y^+ \sim 17$ in the near-wall region and $y^+ \sim 600$ in the outer layer. The inner peak of the turbu-
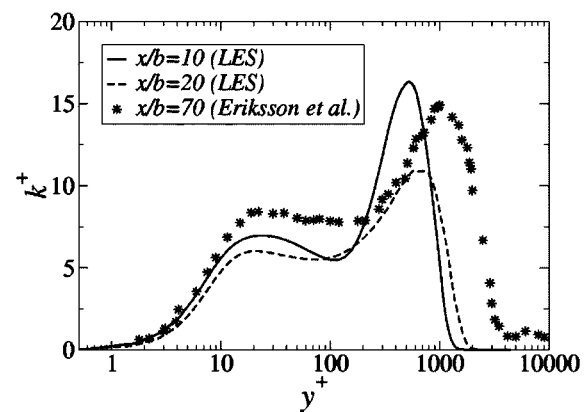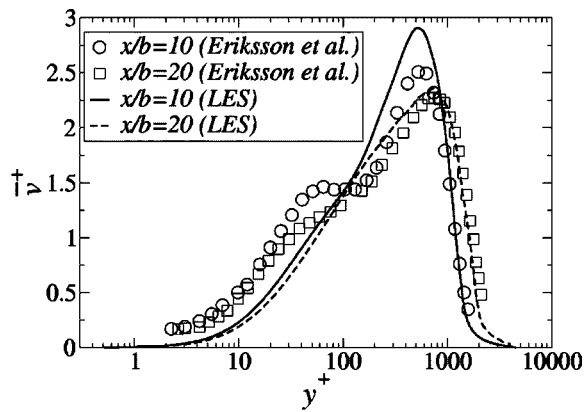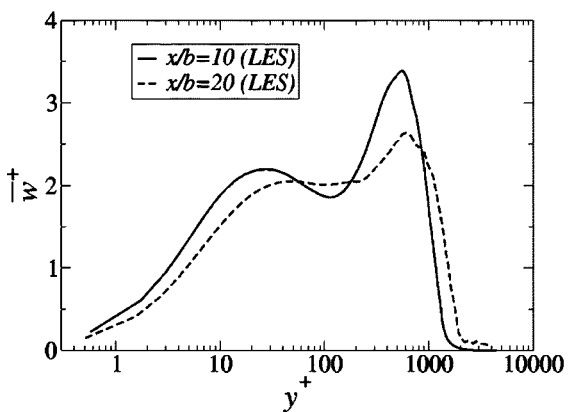

FIG. 13. Profiles of the rms of normal stresses and of turbulence energy at the locations $x/b = 10$ and 20, scaled with inner variables.
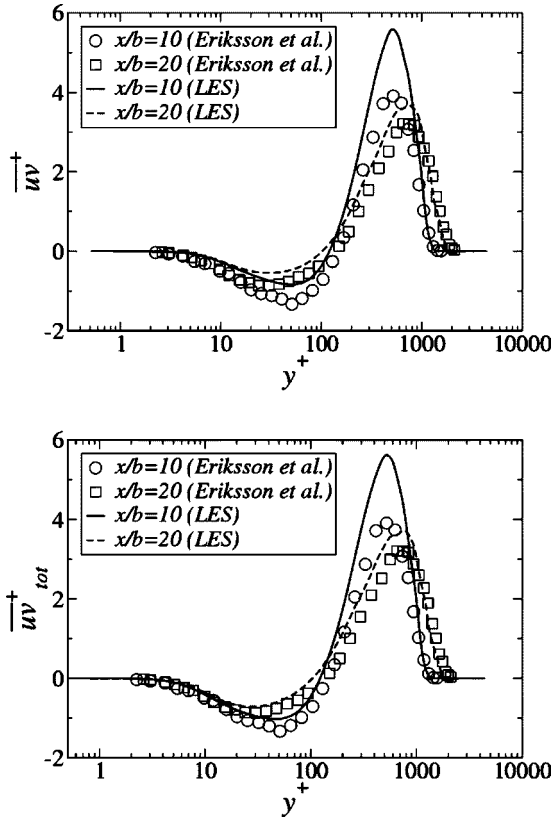
FIG. 15. Profiles of the resolved and total shear stress at the locations $x/b = 10$ and 20, scaled with inner variables.

FIG. 16. Profiles of the triple velocity correlations, scaled with inner variables.

lence intensity is located at a wall distance comparable to that in a standard boundary layer. The transverse normal fluctuation $\bar{v}^+$ is well predicted in the outer shear layer, but the plateau observed in the interaction region is not reproduced by the LES at the stations considered. This difference was observed in all simulations undertaken, regardless of the subgrid-scale model and the grid employed (it is recalled that 40 grid cells are placed in the range $0 < y^+ < 100$). The much lower near-wall level of $\bar{v}^+$ relative to $\bar{w}^+$ is due to wall-blocking acting on the former. Eriksson *et al.* report that the near-wall plateau of v^+ only arises in the near-field and tends to disappear in the fully self-similar region. This trend is indeed observed when comparing the $\bar{v}^+$ profiles measured at the locations $x/b = 10$ and $x/b = 20$. That the plateau is also present in the simulation is demonstrated in Fig. 14, which contrasts $\bar{v}^+$ at $x/b = 8$ and 20. It thus appears that the simulation gives a faster decay of the plateau, rather than missing it. The origin of this misrepresentation is not clear, but presumed to be linked to the transition in the near-wall layer. As noted already, a faithful representation of the near-wall transition is difficult to achieve. While the grid is especially fine in this region ($18 < \Delta x^+ < 24$ and $0.4 < y_1^+ < 0.6$), some grid-resolution and subgrid-scale-modeling effects cannot be excluded. Added to this, the transitional behavior also depends on the inlet flow, including its spectral properties. Near-wall transition involves very fine structures, the resolution of which is considerably more challenging than that of the large-scale structures arising in the transition in the separated shear layer. However, simul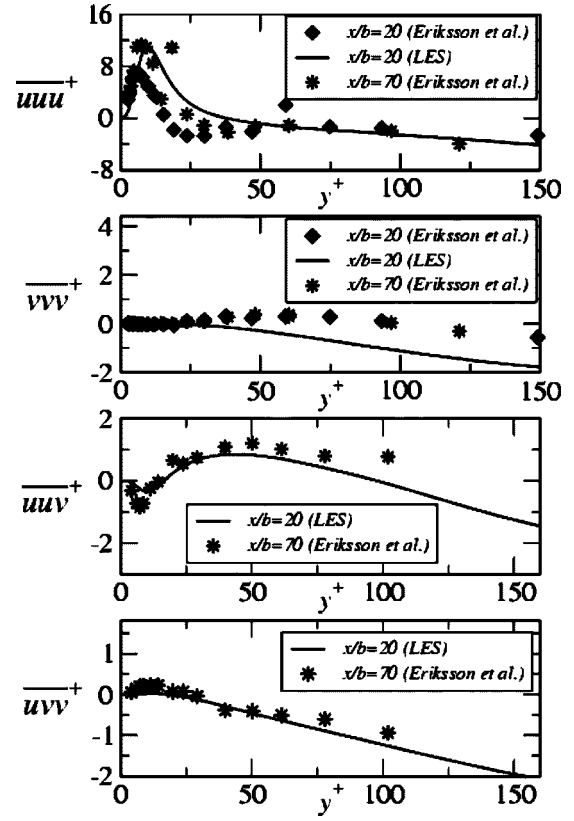ations performed with a sequence of grids coarser than the one for which results are reported herein and with different subgrid-scale models did not show a trend towards an improved representation of the near-wall peak in $\bar{v}^+$. Hence, the faster decay in the peak of $\bar{v}^+$ in the simulation cannot be attributed unambiguously to under-resolution on the basis of the available information. It is noted that $\bar{v}^+$ is lower than the experimental level only below $y^+ = 80$; the level of anisotropy is thus broadly correct. In the same range, the computed $\bar{u}^+$ does not exceed the experimental level, especially not in the near-wall region. Beyond $y^+ = 80$, $\bar{v}^+$ and $\bar{u}^+$ at $x/b = 10$ are both slightly higher than the respective experimental data. These observations, taken together, may be claimed to indicate that there is no significant under-resolution over most of the flow in this region, a defect that is often observed to be the cause of excessive anisotropy in channel-flow LES.

As regards the comparisons of turbulence-energy profiles, given in Fig. 13, it should be noted that the predicted profiles at $x/b = 10$ and 20 are compared with experimental data at $x/b = 70$, because of the absence of full measurements (in particular $\bar{w}^+$ further upstream. Despite this difference in location, the comparison may be defended on the grounds that self-similarity is effectively achieved at $x/b = 10$, so that inner scaling should collapse the data close to the wall. The comparison thus indicates that the location of the energy peak, $y^+ \sim 20$, which is close to the inner peak of $\bar{u}^+$, compares well with the experiment.

Profiles of the resolved and total Reynolds shear stress are shown in Fig. 15. A comparison of corresponding distri-

butions reveals only a slight contribution of the subgrid-scale stress, and this only in the near-wall region $10 < y^+ < 100$. The predicted profile at $x/b = 20$ agrees fairly closely with the experimental variation, but there is a tendency for the computed (nondimensional) stress to be too high, especially at $x/b = 10$. This is due, mainly, to the fact that the predicted wall-shear stress is lower than that measured. In addition, differences in the transitional behavior have a significant impact on the streamwise evolution of the shear-stress field, thus also contributing to the observed differences, especially at $x/b = 10$. The computed shear stress vanishes at $y^+ = 102.5$, while the shear strain vanishes at $y^+ = 137$. This dislocation is a well-known feature of the wall jet and implies a substantial level of shear-stress transport in the interaction region. The principal contribution to this transport arises from gradients of the triple velocity correlations. While these will be considered as part of the discussion of stress budgets, to follow later, measured data for the correlations, $\overline{uuu}^+$, $\overline{uuv}^+$, $\overline{uvv}^+$, and $\overline{vvv}^+$ allow a limited direct assessment of this important element of the stress budget to be undertaken here. The limitation is posed by the fact that almost all the measurements for the triple correlations have been performed in the fully self-similar region of the flow, well beyond the streamwise extent of the computational domain ($x/b = 70$); only the correlations $\overline{uuu}^+$ and $\overline{vvv}^+$ are directly comparable to the LES results at the location $x/b = 20$. Nevertheless, the comparison between the simulation data and measurements at $x/b = 70$, is essentially valid and defensible, because the flow can be regarded as almost self-similar beyond $x/b = 20$. This comparison is thus presented in Fig. 16. Of particular interest are the correlations involving both u and v, because their wall-normal gradients contribute significantly to the budgets. The profiles of $\overline{uuu}^+$ and $\overline{vvv}^+$ measured at $x/b = 20$ and 70 indicate only a slight evolution of the triple correlations beyond $x/b = 20$. The location of the minimum in $\overline{uuv}^+$, at the distance $y^+ \sim 10$, compares well with the experimental locations $y^+ \sim 7$. Similarly, the experimental maxima of $\overline{uuv}^+$ and $\overline{uvv}^+$ at $y^+ \sim 50$ and $y^+ \sim 12$, respectively, are reproduced broadly correctly, as are the zero-crossing of these correlations. However, the predicted magnitude of both correlations tends to be lower than that of the measurements, which is consistent with the relatively low transverse intensity $\overline{v}^+$ returned by the simulation near the wall. An insufficient level of transverse fluctuations close to the wall is also implied by the $\overline{vvv}^+$ profile. The profile of $\overline{uuu}^+$ follows well the experimental variation, with a peak in the near-wall region that is located slightly above the measurements and is a little larger in magnitude. The minimum observed in the experiments at the location $x/b = 20$, just beyond the peak, is not reproduced by the LES which provides a $\overline{uuu}^+$ profile closer to the measurements at $x/b = 70$, where the minimum is much less pronounced.

As will be shown later, the transport terms containing the triple correlations play an especially important role in the budgets for the shear stress and wall-normal intensity over the range covering the interaction region. The particular terms at issue are the wall-normal gradients of $\overline{uvv}^+$ and $\overline{vvv}^+$. Although the agreement in Fig. 16 is far from perfect, the y-wise *gradient* of these correlations falls in the range of
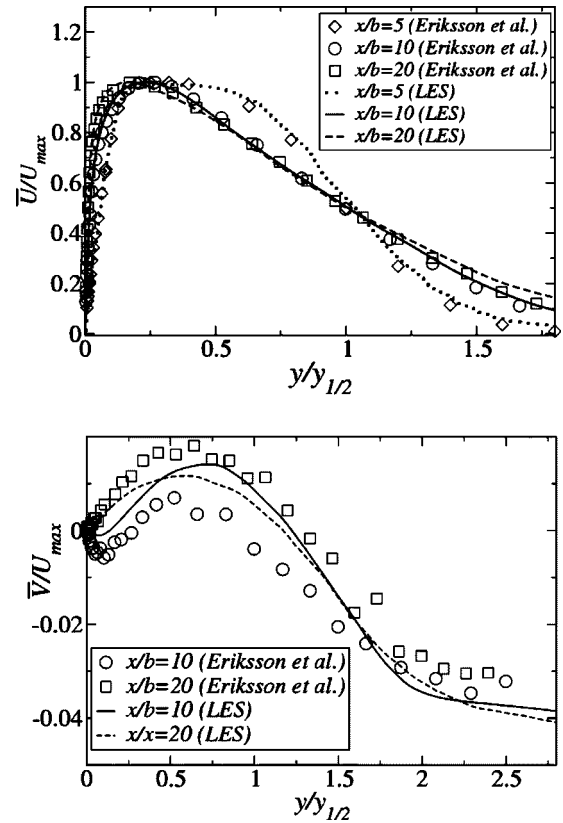

FIG. 17. Profiles of the streamwise and the wall-normal velocity at the locations $x/b = 10$ and 20, scaled with outer variables.

values given by the experiment in the self-similar region of the jet. It is this gradient that identifies stress transport in the stress budgets. For both stresses, the variations of the triple correlations imply stress gains in the respective budgets, and this is indeed what the budgets will reveal.

B. Outer-scaled property variations

Outer scaling is appropriate, in principle, for identifying a self-similar behavior of the outer shear layer, and this is the rationale underpinning the presentation provided in this section. However, as noted earlier, the shear stress in the outer layer depends on the Reynolds number, especially at the low values pertaining to the near-field, and so do, therefore, other properties in the outer region.

Mean-velocity and turbulence data, scaled with U_{max} and $y_{1/2}$, are presented on Figs. 17–19. Excellent agreement with the experiments is observed for the streamwise velocity profiles throughout the domain of computation, including the early transitional region at $x/b = 5$. Similarly, the wall-normal velocity profile and the Reynolds-stress profiles compare well with the experiments in the region $0 < y/y_{1/2} < 0.5$, but there are some discrepancies in the range $0.5 < y/y_{1/2} < 1.5$. In this region, the shear stress at $x/b = 10$ is higher than the experimental level. This behavior was also observed earlier, when the shear stress was scaled in terms of inner variables. In fact, the differences were considerably larger than those seen in Fig. 18, and these were attributed, principally, to the simulation returning an insufficient wall-shear stress. From
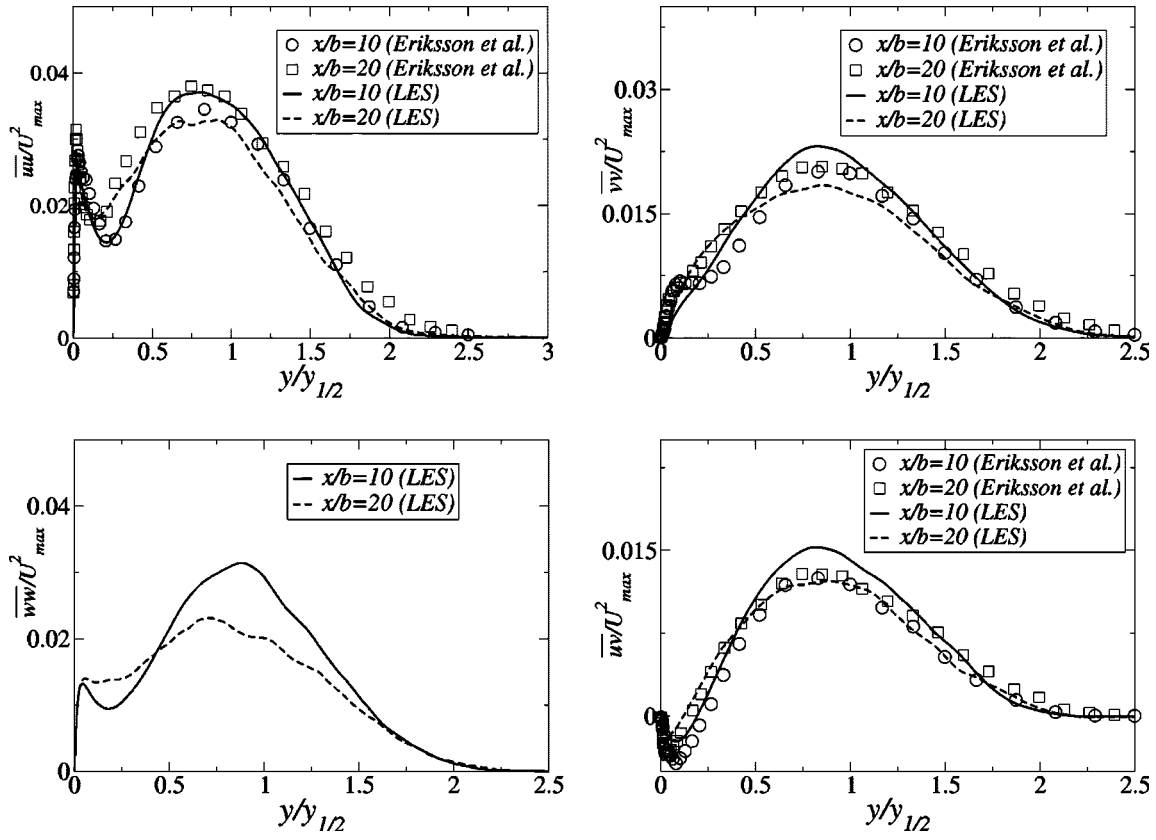
FIG. 18. Profiles of shear and normal stresses at the locations $x/b=10$ and 20, scaled with outer variables.

the present comparison, it is evident that the actual shear stress is also too high. However, the fact that the shear stress at $x/b=20$, scaled with outer variables, is correct, while that scaled with inner variables is still too high, gives support to the assertion made earlier that transitional aspects contribute to the shear-stress differences at $x/b=10$. The general behavior observed in the computed fields in the outer region is that the wall-normal velocity as well as the turbulence quantities are somewhat higher in the transitional region than in the self-similarity region. This behavior is contrary to that observed in the measurements for the wall-normal velocity, $\bar{V}/U_{\max}$, and the streamwise normal stress, $\overline{uu}/U_{\max}^2$. It is

furthermore seen from Fig. 18 that the measured wall-normal and shear stresses, $\overline{vv}/U_{\max}^2$ and $\overline{uv}/U_{\max}^2$, exhibit negligible streamwise variations in the central region between the locations $x/b=10$ and 20, while the simulation returns a slight decrease. This decrease is even more pronounced when the shear stress is plotted in terms of the scaling proposed by George et al., as done in Fig. 19. What this figure also shows is that the measured shear stress, when normalized by u_τ^2, reduces as well. Thus, the simulation reproduces, qualitatively correctly, the experimental behavior in terms of the streamwise variation of the shear stress when this is appropriately scaled.
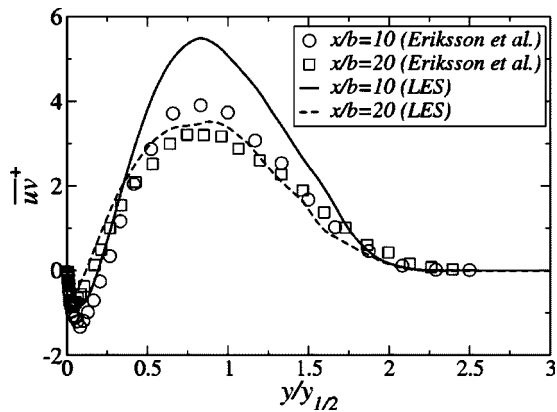

FIG. 19. Profiles of the shear stress at the locations $x/b=10$ and 20, scaled according to George et al. (Ref. 12).

V. BUDGETS OF TURBULENCE ENERGY AND REYNOLDS STRESSES

As noted in the introduction, a major objective of the present study is to extract and interpret the budgets of the Reynolds stresses, for these arguably provide the key to understanding the behavior of the second moments, and thus form the foundation for improving turbulence closures. In the case of the wall jet, a particularly interesting question is whether the budgets can shed light on what mechanisms play a prominent role in the interaction between the boundary layer and the outer flow.

The equations expressing the budgets of the turbulence

energy and the Reynolds stresses of the resolved scales are, respectively,

$$\frac{\partial k}{\partial t} + \bar{U}_j k_{,j} = \underbrace{-\overline{u_i u_j} \bar{U}_{i,j}}_{P} + \underbrace{\nu k_{,jj}}_{D_\nu} \underbrace{-\left(\overline{u_j \frac{u_i u_i}{2}}\right)_{,j}}_{TTT} \underbrace{-\left(\overline{\frac{p}{\rho} u_j}\right)_{,j}}_{\Pi}$$

$$\underbrace{-\nu \overline{u_{i,j} u_{i,j}}}_{\varepsilon_c} + \text{SGS contributions}$$

$$\underbrace{}_{\text{balance} = \varepsilon} \tag{3}$$

$$\frac{\overline{\partial u_i u_j}}{\partial t} + \underbrace{\bar{U}_k \overline{u_i u_j}_{,k}}_{C_{ij}} = \underbrace{-\overline{u_k u_j} \bar{U}_{i,k} - \overline{u_k u_i} \bar{U}_{j,k}}_{P_{ij}} + \underbrace{\nu \overline{u_i u_j}_{,kk}}_{D_\nu} \underbrace{- \overline{u_i u_j u_k}_{,k}}_{TTT_{ij}}$$

$$\underbrace{-\frac{\overline{(u_j p_{,i} + u_i p_{,j})}}{\rho}}_{\Pi_{ij}} \underbrace{- 2\nu \overline{u_{i,k} u_{j,k}}}_{\varepsilon_{c_{ij}}} + \text{SGS contributions}$$

$$\underbrace{}_{\text{balance} = \varepsilon_{ij}} \tag{4}$$

where $k = \frac{1}{2}\overline{u_i u_i}$. In the above, the symbols below the underbraces designate the specific budget contributions plotted in figures to follow.

It is recalled here that the dissipation rate is not evaluated explicitly from the filtered field, but from the balance of the other terms, as is indicated in Eqs. (3) and (4). It therefore represents the total level of dissipation, including the viscous and subgrid-scale part. The admissibility of doing so is justified by the fact that the effect of the subgrid scales is essentially dissipative, while their contribution to all remaining terms in the stress-balance equation is insignificant, as these terms are entirely dominated by the large-scale dynamics. This is further clarified upon expressing the dissipation rate of the turbulence energy in terms of the filtered-field and the subgrid-scale contributions:

$$\underbrace{\varepsilon}_{\text{balance}} = \left(-\nu \overline{u_{i,j} u_{i,j}}\right) + \overline{\tau_{ij} \bar{u}_{i,j}} - \overline{(\tau_{ij} u_i)}_{,j} \tag{5}$$

where τ_{ij} denotes the subgrid-scale stress tensor. In the present LES, the cut-off is located well within the dissipative scales of turbulence, so that the total turbulence energy is $k = k_r + k_{sgs} \sim k_r$, where k_{sgs} and $k_r = 0.5\overline{u_i u_i}$ are, respectively, the subgrid-scale and resolved components. It then follows that the term $\overline{\tau_{ij} u_j} \sim \mathcal{O}(k_{sgs}\sqrt{k})$ is small compared to the term $\overline{u_i u_i u_j} \sim \mathcal{O}(k^{3/2})$. Thus, the turbulent transport of the subgrid-scale stresses can be neglected, and the balance of Eq. (3) will include mainly the subgrid-scale dissipation $\overline{\tau_{ij} u_{u,j}}$. Similar conclusions can be deduced for Eq. (4).

The budgets for the location $x/b = 20$ are presented in Figs. 20–24. In Fig. 20 the budget for the turbulence energy is presented in two parts: that for the near-wall region is scaled with the inner variables, while that for the outer layer is scaled with the outer variables. Some of the profiles in the latter are considerably less smooth than those in the former, reflecting the prevalence of large scales in the intermittent outer flow. However, the distributions nevertheless provide an adequate view of the processes they represent. To increase smoothness further, a longer integration time, well beyond the 20 flow-through periods used, would be required. This was not done purely because of resource limitations.
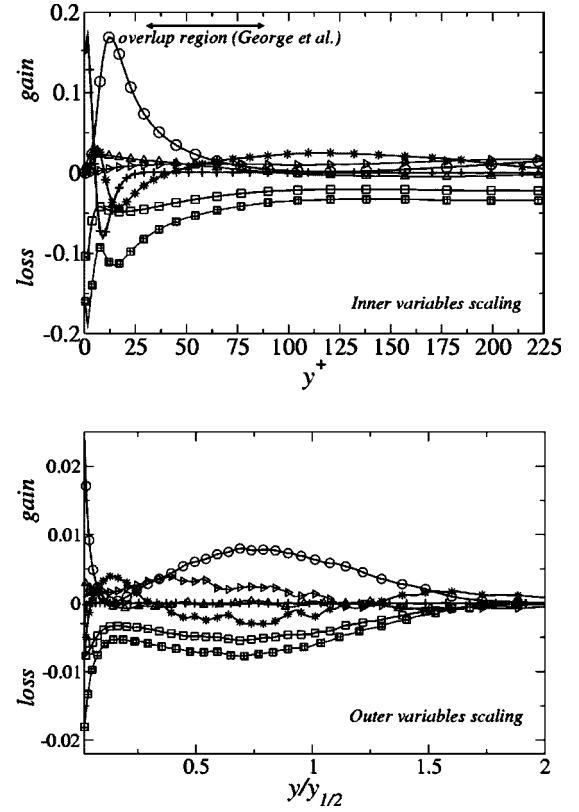

FIG. 20. Budget of the turbulence kinetic energy [see Eq. (3)] at the location $x/b = 20$. Top: normalized by u_τ^4/ν. Bottom: normalized by $U_{\max}^3/y_{1/2}$. The dissipation term ε_c is the computed one and the dissipation term ε is deduced from the balance. $\bigcirc$-$\bigcirc$: P; $\triangleright$-$\triangleright$: C; $+$-$+$: D_ν; $\square$-$\square$: ε_c; $*$-$*$: TTT; $\triangle$-$\triangle$: Π;; $\boxplus$-$\boxplus$ ε.

In the near-wall region, the budget of the turbulence energy presents the usual features observed in a normal boundary layer: beyond the viscous sub-layer, the production is balanced by dissipation and, to a lesser extent, by turbulent diffusion; very close to the wall, the dissipation is balanced by viscous diffusion, in accordance with the wall-asymptotic form of the turbulence-energy equation; within the buffer region, where production reaches a maximum, viscous and turbulent diffusion rise steeply to effect the transport of turbulence energy away from the region of maximum production towards the wall and the outer region; and finally, convection is insignificant. The dissipation rate is seen to reach a peak value of approximately 0.19. This differs significantly from the value 0.27 reported by Eriksson, albeit at $x/b = 70$. However, Eriksson estimated his value from the wall-asymptotic variation of the turbulence-intensity components, measured in the region $1 < y^+ < 10$, and inserting this into the viscous-diffusion term that balances the near-wall dissipation. Applying the same approach to the simulated intensity distributions yields a wall-dissipation value of 0.22. Thus, both methods of evaluation, from the budget and from asymptotic considerations, give quite different values for the wall dissipation. This may be attributed to the very steep variation in the turbulence-energy diffusion very close to the wall, which makes the asymptotic analysis rather inaccurate.

In the outer region, the budget of the turbulence energy contains all the features characteristic of a free shear flow.
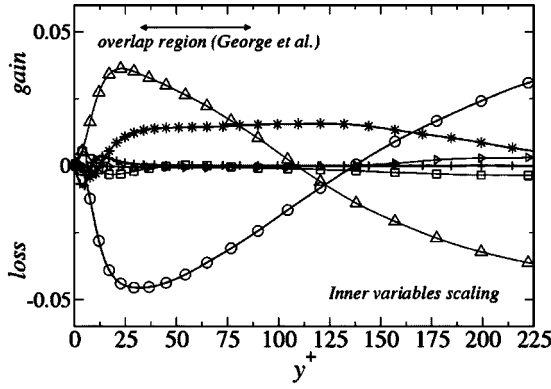
FIG. 21. Budget of the shear stress [see Eq. (4)] at location $x/b=20$. Top: normalized by u_τ^4/ν. Bottom: normalized by $U_{\max}^3/y_{1/2}$. The dissipation term ε_{uv} is deduced from the balance. O-O: P_{uv}; ▷-▷: C_{uv}; +-+: D_ν; *-*: TTT_{uv}; △-△: Π_{uv};; □-□: ε_{uv}.

FIG. 22. Budget of the streamwise normal stress [see Eq. (4)] at the streamwise location $x/b=20$. Top: normalized by u_τ^4/ν. Bottom: normalized by $U_{\max}^3/y_{1/2}$. The dissipation term ε_{uu} is deduced from the balance. O-O: P_{uu}; ▷-▷: C_{uu}; +-+: D_ν; *-*: TTT_{uu}; △-△: Π_{uu};; □-□: ε_{uu}.

The principal balance is between production and dissipation. Convection and turbulent diffusion make relatively minor contributions, the former transporting turbulence energy forward from upstream regions, while the latter transporting energy laterally from the high-production, outer portion of the jet towards inner regions, including the interaction layer. In the interaction region, the most striking feature is the high level of turbulent transport. Here, production is low, almost vanishing at $y^+=125$, but remaining positive throughout, in accord with observations by Irwin[5] and Eriksson.[11] The significant level of dissipation is balanced by turbulent transport, arising from both the wall and the core of the jet, and by convection from upstream regions.

The budget for the shear stress is shown in Fig. 21. Again, the near-wall region features characteristics that are similar to those in a boundary layer: Dissipation is insignificant, characterizing isotropy in the smallest scales; the high level of (negative) shear production is balanced by the velocity-pressure correlation and, to a lesser extent, by turbulent diffusion transporting stress away from the high-production area; all remaining terms make insignificant contributions. In the outer region, positive production is nearly balanced by the velocity-pressure term. The interaction layer is here of particular interest, especially in view of George *et al.*'s[12] conclusions on the relevance of the inner variable u_τ to the scaling of $\overline{uv}$ in the outer region. The most important feature to highlight is the role of turbulent diffusion over the range $y^+\sim 30$ to $y^+\sim 220$. As indicated in Fig. 21, this range
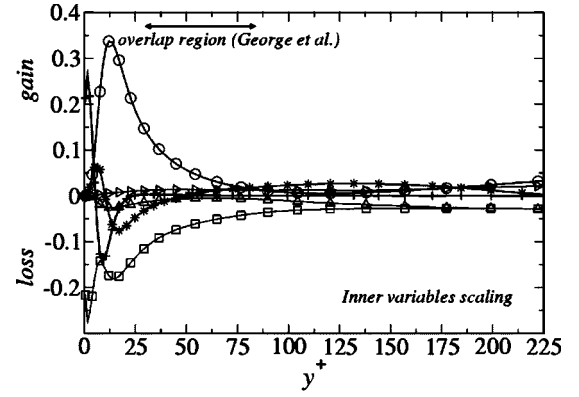
contains the interaction region defined according to George *et al.* The role of turbulent diffusion is also well brought out in the budget scaled with outer variables, also given in Fig. 21. This clearly shows the dominance of stress transport in the layer extending to $y/y_{1/2}=0.3$. Reference to the budget scaled with the inner variables, shows that the production vanishes at $y^+=135$, which corresponds to the position of vanishing shear strain. The shear stress itself vanishes at $y^+=102.5$. At this location, the velocity-pressure term is insignificant, and the production, being substantially negative, in consonance with the positive shear strain, is balanced mainly by turbulent diffusion. Here, this diffusion tends to counteract the production-induced elevation of the shear-stress magnitude by transporting shear stress into this region from the positive-stress outer layer; hence, the shift of the zero shear-stress location towards the wall. This transport is evidently influential right down to the viscous sublayer. Moreover, the outer layer is evidently influenced by the inner layer well beyond $y/y_{1/2}=0.5$. It thus follows that a realistic modeling of shear-stress transport (or its effects) is one key aspect of securing an adequate turbulence-model performance in the wall jet. Indeed, this conclusion is likely to extend to any near-wall flow that features an interaction between two disparate flow regions in terms of their origin and evolution prior to their interaction.

The budgets for the normal stresses are given in Figs. 22–24. That for the streamwise stress is, as expected, similar to the turbulence-energy budget. The only important point of
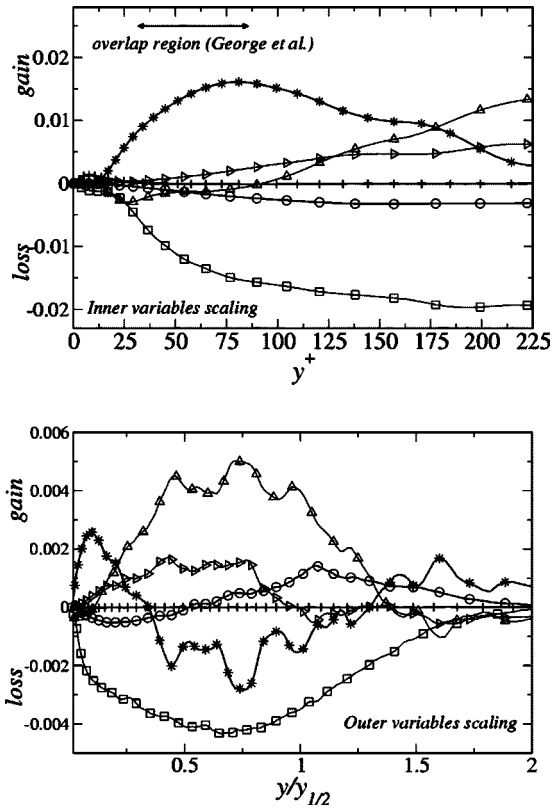
FIG. 23. Budget of the transverse normal stress [see Eq. (4)] at the streamwise location $x/b=20$. Top: normalized by u_τ^4/ν. Bottom: normalized by $U_{max}^3/y_{1/2}$. The dissipation term ε_{vv} is deduced from the balance. $\bigcirc$-$\bigcirc$: P_{vv}; $\triangleright$-$\triangleright$: C_{vv}; $+$-$+$: D_ν; $*$-$*$: TTT_{vv}; $\triangle$-$\triangle$: Π_{vv};; $\square$-$\square$: ε_{vv}.

FIG. 24. Budget of the spanwise normal stress [see Eq. (4)] at the streamwise location $x/b=20$. Top: normalized by u_τ^4/ν. Bottom: normalized by $U_{max}^3/y_{1/2}$. The dissipation term ε_{ww} is deduced from the balance. $\bigcirc$-$\bigcirc$: P_{ww}; $\triangleright$-$\triangleright$: C_{ww}; $+$-$+$: D_ν; $*$-$*$: TTT_{ww}; $\triangle$-$\triangle$: Π_{ww};; $\square$-$\square$: ε_{ww}.

difference is the role of the velocity-pressure correlation, which partially compensates for the production substantially exceeding dissipation by transferring energy from the streamwise component to the other normal stresses. Interestingly, the velocity-pressure term makes a relatively minor contribution in the inner layer, in comparison to the turbulent diffusion, which transports turbulence away from the high-production region towards the outer region and the wall. Here again, this is a feature which reflects the strength and extent of the interaction between the two layers. This is emphasized in the near-wall budget for $\overline{vv}$, which is dominated by a balance between dissipation and turbulent diffusion. The velocity-pressure correlation tends to elevate $\overline{vv}$ away from the wall, as energy is transferred to it from $\overline{uu}$, but within $y^+ \sim 100$, the contribution of this process is unusually low. In fact, contrary to the behavior in an ordinary boundary layer (see Mansour et al.[26]), the velocity-pressure term does not exhibit a positive peak, but is very low and features a slight negative trough in the region $y^+ \sim 25-30$. This substantially different behavior is induced by the high level of turbulent diffusion from the high-shear zone of the jet towards the interaction region up to the wall, and the need for the wall-normal stress to diminish rapidly so as to steer the turbulence field towards a two-component state at the wall. The role of turbulent diffusion is also brought out clearly in the budget scaled with the outer variables. As seen, turbulent diffusion is the dominant mechanism over a large portion of the near-wall region, extending well into the outer layer. Away from
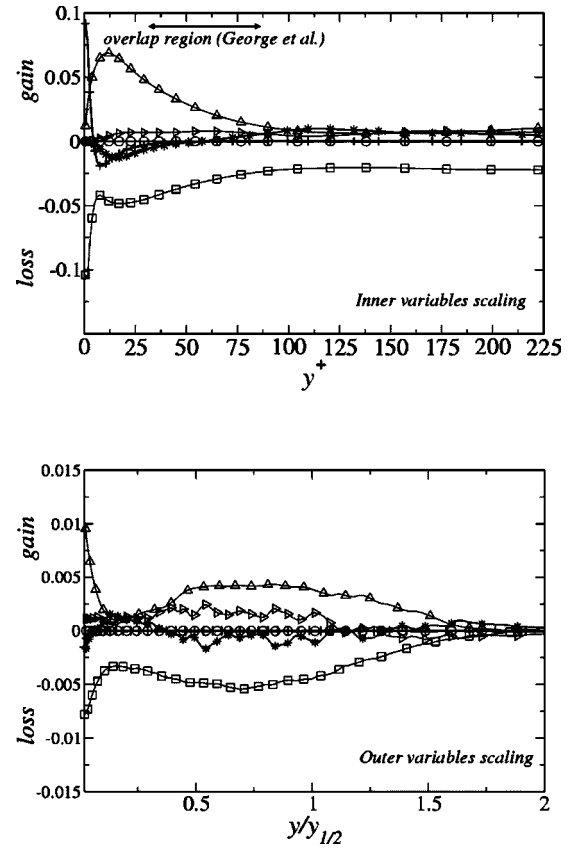
the interaction region, the balance is mainly between dissipation and the velocity-pressure correlation, the latter promoting isotropization, as is observed in any free shear flow. The near-wall budget for the spanwise normal stress shows the more familiar role of the velocity-pressure correlation balancing dissipation. As in the case of the turbulence energy and the streamwise stress, dissipation is balanced by viscous diffusion at the wall. In the interaction region, turbulent diffusion is again influential, but its importance is here diminished by the contribution of the velocity-pressure correlation, which remains significantly positive in this region. In the outer layer, well away from the interaction region, dissipation is balanced mainly by the velocity-pressure term, which is similar in intensity to that pertaining to the wall-normal stress $\overline{vv}$. Hence, in this region, the flow behaves essentially like an ordinary free shear layer.

In the light of the above observations on the exceptional importance of turbulence transport in the interaction region, it is interesting to examine the ratio of turbulence-energy production, P, to its dissipation, ε, in order to identify more clearly the relative role of transport. The variation of the ratio P/ε is shown in Fig. 25, both against the outer-scaled and inner-scaled distances, $y/y_{1/2}$ and y^+, respectively. This ratio is approximately unity over the range $y/y_{1/2} > 0.75$, which corresponds to the outer shear layer. In the inner region, however, this ratio varies strongly, and in a manner substantially different from that observed in a standard near-
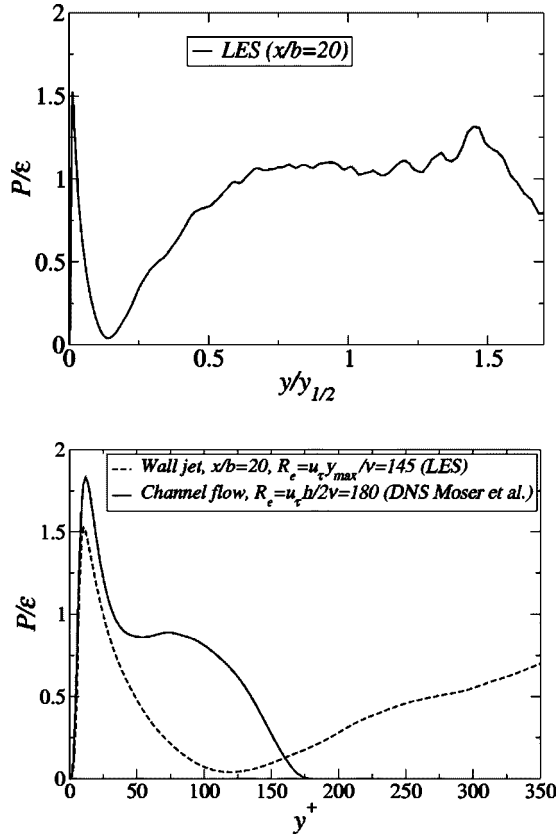
FIG. 25. Top: ratio of production P to dissipation ε of turbulence energy at the location $x/b=20$. Bottom: comparison of P/ε for the turbulent channel flow and the turbulent wall jet.

FIG. 26. Top: realizability map for the turbulent wall jet at the location $x/b=20$. Bottom: realizibility map for the equivalent fully-developed turbulent channel flow.

wall layer. To demonstrate this, the variation of P/ε for the wall jet is compared to that in a fully developed channel flow at the Reynolds number, $Re_{\tau,h}=u_\tau h/2\nu=180$, h being the channel half-height, obtained from a DNS by Moser et al.[27] This value of $Re_{\tau,h}$ is close to $Re_{\tau,y_{max}}=u_\tau y_{max}/\nu=145$ found in the self-similar region of the present wall jet, where y_{max} is the distance to the location $U=U_{max}$. Very near to the wall, the wall jet and the channel flow exhibit similar behavior. In the log-law region of the channel flow, $50<y^+<100$, the ratio P/ε is, as expected, close to unity, reflecting equilibrium. A very different behavior is presented by the wall jet, however. The production has to practically vanish close to the location of zero shear strain, i.e., around $y^+=120$. The near-wall region thus contains a thin layer in which the log-law broadly applies (Fig. 12). However, even in this region the ratio P/ε is far below unity. This level is only recovered as the interaction region merges into the outer free-shear layer. Thus, in the region within which the near-wall layer interacts with the inner part of the free shear layer, the flow is far from equilibrium, due to the important contribution made by the turbulence diffusion from the outer region towards the wall.

Finally, in order to accentuate the contrast between the near-wall region of the wall jet and the channel flow, Fig. 26 compares anisotropy ("realizability") maps for a fully turbulent channel flow at $R_{\tau,h}=180$ and the turbulent wall plane jet. The maps relate to the second invariant $II=1/2b_{ij}b_{ij}$ to
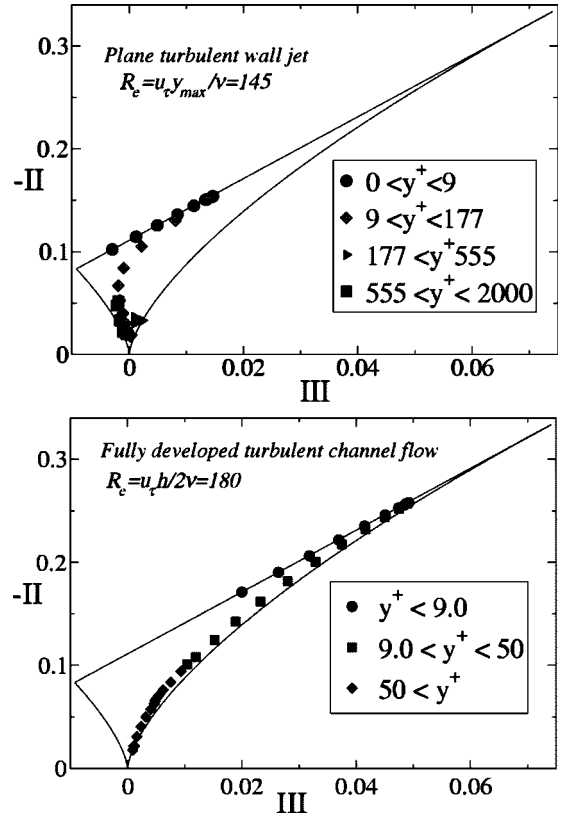
the third invariant $III=1/3b_{ik}b_{kj}b_{ji}$, where $b_{ij}=\overline{u_i u_j}/2k -1/3\delta_{ij}$. The symbols in the maps identify II-III loci as the flow is traversed in the wall-normal direction. Very near to the wall, both flows follow the two-component-turbulence lines, while both approach the isotropy point far away from the wall. The behavior between these two limiting states differs greatly, however. In the channel flow, the alignment with the *axisymmetric-expansion* line, the lower right-hand-side of the triangle, is characteristic of the log law. In contrast, the turbulent state in the wall jet tends to follow the *axisymmetric-contraction* line, which is characteristic of a free shear layer. This is broadly the expected behavior, because much of the wall jet consists of a "free" shear layer, only part of which is affected by the wall.

VI. LENGTH AND TIME SCALES

Figure 27 shows wall-normal variations of the turbulent length scale $l_\varepsilon=k^{3/2}/\varepsilon$, normalized in two ways: one by reference to the wall variables, u_τ and ν, and the other by reference to the equilibrium value of the length scale $C_\mu^{-3/4}\kappa y$, where $C_\mu=0.09$ and $\kappa=0.41$. The length scale computed for the jet is compared to that derived from Moser et al.'s[27] DNS data for a channel flow at $Re_{\tau,h}=180$. An analogous comparison for P/ε has already been presented in Fig. 25, with the rationale explained in Sec. V.

As seen from Fig. 27, the behavior of the length scale in the near-wall layer of the jet differs substantially from that in the channel. In particular, the former is considerably larger,

FIG. 28. Time scale normalized by the wall variables, u_τ and ν, at the location $x/b=20$.
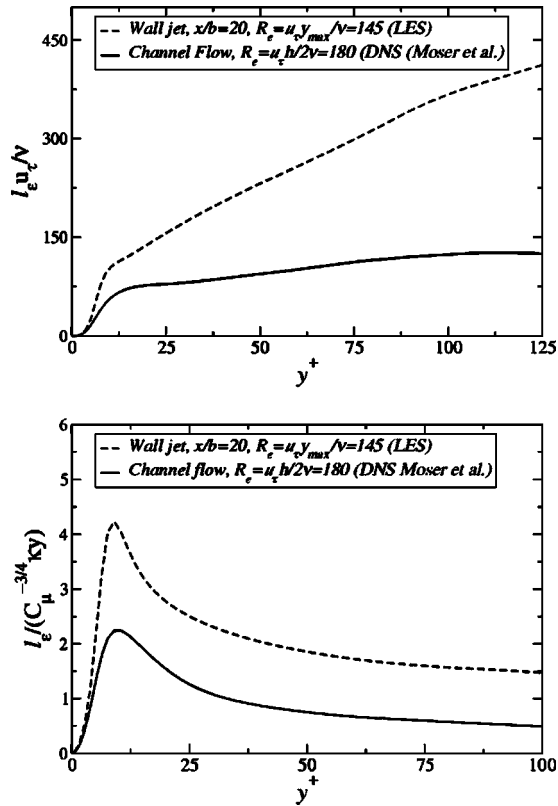

FIG. 27. Top: dissipation-length scale normalized by wall variables at the location $x/b=20$. Bottom: dissipation-length scale normalized by the equilibrium length scale at the location $x/b=20$.

rises much more steeply with the wall distance and does not conform in any part of the near-wall region to the equilibrium level. As the interaction region in the jet begins at $y^+ \sim 80$, the length scale beyond this location can be expected to be increasingly affected by the large scales in the outer shear layer. However, the variations shown in Fig. 27 demonstrate that the entire near-wall layer is affected by the outer flow. Despite the existence of a mean-velocity layer in the range $28 > y^+ > 80$ that conforms broadly to the log law (Fig. 12), the departure of the length scale in this layer from the equilibrium level is not surprising, in view of the variation of P/ε, shown in Fig. 25. Specifically, turbulence production is seen to be low in this layer, and the budget shows that the dissipation rate is balanced principally by diffusion from the outer region towards the wall. This diffusion implies, in turn, a migration of energetic outer-layer eddies into the near-wall layer and thus also an elevation of the length scale. In the case of channel flow, the scales in the outer layer are considerably smaller, because of the weakness of production in the central region of the channel.

In contrast to the length scale, Fig. 28 shows the time scale variations in the channel and jet to be fairly similar. This reflects the fact that, in both flows, the dissipation rate follows fairly faithfully the rise in the turbulence energy. While the budget for the turbulence energy shows turbulence transport to be an important contributor to the balance, the sum of transport and production largely balances dissipation, so that the variations of the turbulence energy and dissipation are similar. The rise in the time scale obviously reflects the
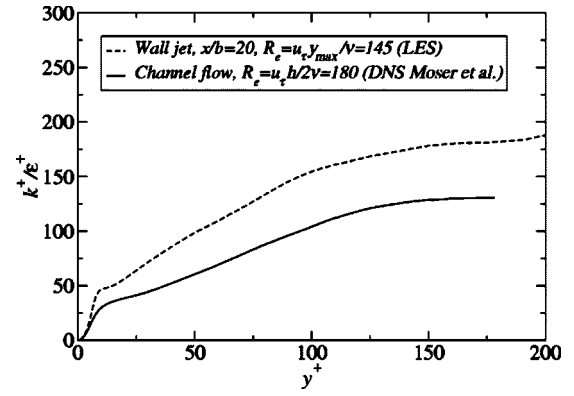
increased length scale and hence the eddy turnover time. One message signalled by Fig. 28 is that a model utilizing a transport equation for the time scale (or its inverse) might be a better foundation for a general closure than one based on a length scale or dissipation-rate equation, at least for flows featuring a strong interaction between disparate flow regimes.

VII. CONCLUSIONS

A highly resolved large eddy simulation of the plane turbulent wall jet has been performed for conditions for which high-quality experimental data are available for cross-examination. The primary objective has been to identify the detailed turbulence mechanisms that govern the global characteristics of the jet. Particular attention has been paid to the self-similar state, the interaction region in which the near-wall layer overlaps with the outer shear layer and related issues of scaling. A distinctive feature of the study is the provision of budgets for Reynolds stresses and turbulence energy. These contribute greatly to the interpretation of the variations of second moments.

Agreement between the solution and the experimental data has been shown to be close in most respects. This applies also to the Reynolds stresses, except for a plateau in the transverse normal stress at around $y^+=100$, which is not reproduced. However, this particular defect has been argued to reflect differences between the predicted and experimental transition processes. Fairly close agreement has also been achieved in respect of the triple correlations.

The analysis of the budgets of the turbulence energy and of the Reynolds stresses highlights the fact that, in the region in which the outer shear layer overlaps with the boundary layer, the turbulent transport is an especially influential mechanism. In this region, the production due to the strain is very low, and dissipation is mainly balanced by turbulent transport and convection. The turbulent transport tends to remove turbulence energy both from the near-wall layer and the outer layer, where production peaks, towards the interaction zone. This region is thus observed to be subjected to a strong input of energy transported by turbulent diffusion. This process manifests itself most clearly in the budget for the cross-flow normal stress and the shear stress. In the prox-

imity of the wall, the velocity-pressure correlation, positive and dominant in a standard boundary layer, is very low and even slightly negative, counteracting the turbulent transport.

The shear-stress budget shows that, at the location at which the shear stress vanishes, the velocity-pressure correlation almost vanishes as well, and that the production is again mainly balanced by turbulent diffusion. This induces the displacement between the zero-shear-stress location and the maximum velocity. In contrast, in the near-wall region, the turbulence energy as well as the streamwise and cross-stream normal stresses are found to be similar to those in a boundary layer, in which, respectively, production by shear stress and gain by pressure-velocity correlation are dominant. However, apart from a very limited portion, the velocity in this layer is far removed from the log law. Moreover, the anisotropy-invariants map suggests that the near-wall flow in the jet, although showing a trend towards that observed in a conventional boundary layer, has a structure which is substantially different from that of the latter.

Finally, an examination of the macro length scale, in comparison with that in channel flow and the equilibrium condition, suggests that, in some respects, the interaction region extends right down to the wall. Specifically, it appears that the length scale in the near wall layer is substantially elevated by the "migration" of large scales from the outer layer towards the wall. This notion is consistent with the observed high level of turbulence-energy diffusion across the interaction region towards the wall, and the relatively low level of production therein.

ACKNOWLEDGMENTS

[1] T. J. Craft and B. E. Launder, "On the spreading mechanism of the three-dimensional turbulent wall jet," J. Fluid Mech. **435**, 305 (2001).

[2] B. E. Launder and W. Rodi, "The turbulent wall jet," Prog. Aerosp. Sci. **19**, 81 (1981).

[3] B. E. Launder and W. Rodi, "The turbulent wall jet-measurements and modeling," Annu. Rev. Fluid Mech. **15**, 429 (1983).

[4] A. Tailland and J. Mathieu, "Jet pariétal," J. Mec. **6**, 103 (1967).

[5] H. P. A. Irwin, "Measurements in a self-preserving plane wall jet in a positive pressure gradient," J. Fluid Mech. **61**, 33 (1973).

[6] I. Wygnanski, Y. Katz, and E. Horev, "On the applicability of various scaling laws to the turbulent wall jet," J. Fluid Mech. **234**, 669 (1992).

[7] M. E. Schneider and R. J. Goldstein, "Laser Doppler measurements of turbulence parameters in a two-dimensional wall jet," Phys. Fluids **6**, 3116 (1994).

[8] B. Abrahamsson, J. Johansson, and L. Löfdhal, "A turbulent plane two-dimensional wall-jet in a quiescent surrounding," Eur. J. Mech. B/Fluids **13**, 533 (1994).

[9] J. G. Eriksson, R. I. Karlsson, and J. Persson, "An experimental study of a two-dimensional plane turbulent wall jet," Exp. Fluids **25**, 50 (1998).

[10] B. Venas, H. Abrahamsson, P. A. Krogstad, and L. Löfdahl, "Pulsed hot-wire measurements in two- and three-dimensional wall jets," Exp. Fluids **27**, 210 (1999).

[11] J. Eriksson, "Experimental studies of the plane turbulent wall jet," Ph.D. thesis, Royal Institute of Technology, Department of Mechanics, Stockholm, Sweden, 2003.

[12] W. K. George, H. Abrahamsson, J. Eriksson, R. I. Karlsson, L. Löfdahl, and M. Wosnik, "A similarity theory for the turbulent plane wall jet without external stream," J. Fluid Mech. **425**, 367 (2000).

[13] G. Gerodimos and R. M. C. So, "Near-wall modeling of plane turbulent jets," J. Fluids Eng. **119**, 304 (1997).

[14] S. Wernz and H. Fasel, "Vortex motion in an unsteady wall forced jet," Phys. Fluids **8**, S11 (1997).

[15] S. Gogineni, M. Visbal, and C. Shih, "Phase-resolved PIV measurements in a transitional plane wall jet: a numerical comparison," Exp. Fluids **27**, 126 (1999).

[16] R. Lardat and M. Leschziner, "A Navier–Stokes solver for LES on parallel computers," Technical Report, Department of Mechanical Engineering, UMIST, 1998.

[17] U. Schumann and R. A. Sweet, "Fast Fourier transforms for direct solution of Poisson's equation with staggered boundary conditions," J. Comput. Phys. **75**, 123 (1988).

[18] H. Schlichting, *Boundary Layer Theory*, 8th ed. (Springer Verlag, Berlin, 1999).

[19] C. F. Neves Bettencourt Da Silva, "The role of coherent structures in the control and interscale interactions of round, plane and coaxial jets," Ph.D. thesis, LEGI, Grenoble, France, 2001.

[20] C. Le Ribault, S. Sarkar, and S. A. Stanley, "Large eddy simulation of a plane jet," Phys. Fluids **11**, 3069 (1999).

[21] S. A. Stanley, S. Sarkar, and J. P. Mellado, "A study of the flow-field evolution and mixing in a planar turbulent jet using direct numerical simulation," J. Fluid Mech. **450**, 377 (2002).

[22] J. Smagorinsky, "General circulation experiments with the primitive equations," Mon. Weather Rev. **91**, 99 (1963).

[23] F. Ducros, F. Nicoud, and T. Poinsot, "Wall-adapting local eddy-viscosity models for simulation in complex geometries," *6th ICFD Conference on Numerical Methods for Fluid Dynamics*, 1998.

[24] M. Germano, U. Piomelli, P. Moin, and W. Cabot, "Dynamic subgrid-scale eddy viscosity model," Phys. Fluids A **3**, 1790 (1991).

[25] P. Bradshaw and M. T. Gee, "Turbulent wall jets with and without an external stream," Aeronautical Research Council R M 3252, 1960.

[26] N. N. Mansour, J. Kim, and P. Moin, "Reynolds-stress and dissipation-rate budgets in a turbulent channel flow," J. Fluid Mech. **194**, 15 (1988).

[27] R. D. Moser, J. Kim, and N. N. Mansour, "Direct numerical simulation of turbulent channel flow up to $Re_\tau=590$," Phys. Fluids **11**, 943 (1999).